Research Square

Preprints are preliminary reports that have not undergone peer review.
They should not be considered conclusive, used to inform clinical practice,
or referenced by the media as validated information.

Polarity-Registered Nuclear Mapping Reveals Discrete Topological Classes of Chromosome Organization

Paolo Netti

paolo.netti@iit.it

Istituto Italiano di Tecnologia https://orcid.org/0000-0002-2435-7181

Luca Messina

Interdisciplinary Research Centre on Biomaterials, University of Naples Federico II
https://orcid.org/0000-0002-8829-8758

Carlo Natale

Interdisciplinary Research Centre on Biomaterials, University of Naples Federico II

Article

Keywords: chromosome territories, nuclear polarity, affine normalization, nuclear architecture, hMSCs, micropatterning

Posted Date: July 30th, 2026

DOI: https://doi.org/10.21203/rs.3.rs-10231463/v1

License: This work is licensed under a Creative Commons Attribution 4.0 International License.
Read Full License

Additional Declarations: There is **NO** Competing Interest.

Abstract

Chromosome organization within the nucleus is tightly linked to gene regulation and cell identity, yet its quantitative comparison across cells remains challenging due to variability in nuclear geometry and orientation. Current approaches largely rely on radial metrics and lack a shared coordinate framework integrating polarity and three-dimensional spatial information. Here, we introduce a polarity-registered and geometrically normalized nuclear coordinate system enabling homolog-resolved mapping of chromosome territories (CTs) across cell populations. By combining affine normalization of nuclear shape with alignment to intrinsic polarity cues, we transform heterogeneous nuclei into a shared spatial reference frame where radial and angular chromosome positions can be directly compared.

Applying this framework to human mesenchymal stem cells (hMSCs), we identify discrete and recurrent nuclear topological classes defined by polarity state, cytoskeletal organization, and homolog-specific chromosome positioning. Homolog-resolved analysis reveals asymmetric spatial behaviors: one homolog maintains stable positioning, whereas the other undergoes polarity-dependent reorganization. Single-cell micropatterning further shows thatgeometric confinement reproducibly stabilizes these topological classes, indicating that defined mechanical and polarity constraints control nuclear organization. This framework enables quantitative classification of nuclear architecture and shows that chromosome organization in adherent cells adopts discrete, reproducible spatial states. This approach provides a foundation for integrating imaging-based spatial genomics with population-level analyses of nuclear organization and cellular heterogeneity.

Introduction

Quantitative comparison of chromosome organization across single cells requires a shared spatial framework that integrates nuclear morphology, polarity, and three-dimensional genome architecture. The spatial arrangement of chromatin within the nucleus is tightly linked to gene regulation[1], DNA replication[2], repair[3], recombination[4], differentiation[5], and responses to mechanical and biochemical cues[4]. Chromosomes occupy distinct territories (CTs) that emerge from hierarchical chromatin folding into compartments and higher-order domains[6–8]. Although CTs display non-random positioning patterns, such as the preferential radial localization of gene-rich versus gene-poor chromosomes[9–13], most analyses interpret nuclear organization using simplified spherical and predominantly radial models. These approaches do not account for the geometric and polarity-driven variability of adherent cells, limiting rigorous cross-cell comparison and potentially obscuring higher-order topological relationships among chromosomes.

A wide range of experimental strategies has been developed to interrogate three-dimensional genome organization[14–16]. Imaging-based methods, including fluorescence in situ hybridization (FISH), enable direct visualization of CT positioning[17–19], while chromosome conformation capture 3C-based methods quantify genome-wide interaction frequencies[20–23]. More recently, sequencing-based approaches such

as GPSeq have extended these analyses by inferring chromatin depth relative to the nuclear periphery[24]. Despite these advances, most methods still rely primarily on radial coordinates[13], lacking a standardized nuclear coordinate system that permits spatial integration of radial and angular information across heterogeneous cell populations. As a result, cross-cell comparisons are often reduced to radial metrics or population-averaged contact maps, potentially masking structured spatial heterogeneity.

This limitation is particularly relevant in adherent cells, where nuclear geometry deviates from spherical symmetry and is strongly influenced by cell shape, cytoskeletal organization, and mechanical constraints[25–31]. Extracellular matrix composition, focal adhesion distribution, cytoskeletal tension[32], and cellular confinement[33] modulate nuclear morphology, chromatin organization[34–38], and chromosome positioning[37–39]. Consequently, genetically identical cells can display pronounced variability in nuclear size, shape, and orientation. Despite this variability, nuclei may share conserved spatial configurations that can be recovered through appropriate geometric transformations. Without a polarity-registered coordinate framework that accounts for this variability, it remains difficult to distinguish stochastic organization from structured and reproducible spatial states.

In this view, CTs from different cells can be aligned into canonical configurations that reveal invariant spatial relationships. This perspective enables the definition of nuclear topological classes as reproducible spatial probability distributions of CTs within a shared coordinate system, rather than as continuous stochastic arrangements.

Here, we introduce a polarity-registered and geometrically normalized nuclear coordinate framework that enables homolog-resolved three-dimensional mapping of CTs across cell populations. By combining affine normalization of nuclear shape with alignment to intrinsic cell polarity cues[40–43], heterogeneous nuclei are transformed into a shared coordinate space in which both radial and angular chromosome positions can be quantitatively compared. We further implement a similarity-based algorithm for population-wide homolog assignment, allowing the reconstruction of coherent homolog-resolved spatial probability maps. Applying this framework to hMSCs as a model of polarity-constrained adherent cells, we uncover discrete and reproducible nuclear topological classes characterized by specific combinations of polarity state, cytoskeletal organization, and homolog-specific chromosome positioning. Using single-cell micropatterning[44–46], we demonstrate that geometric confinement stabilizes these classes, indicating that nuclear topology can be experimentally controlled through defined mechanical and polarity constraints.

This work establishes a generalizable framework for the quantitative classification of nuclear organization and provides a foundation for integrating imaging-based spatial genomics with population-level analyses of nuclear architecture and cellular heterogeneity.

Results

1. Cell adhesion constrains nuclear orientation and defines a common nuclear reference frame

Comparing CTs positioning across cells requires a shared nuclear reference frame defined by three Cartesian axes (x, y, z). In adherent cells, such as hMSCs, this frame can be defined with its origin at the nuclear centroid, the x–y plane parallel to the cell–substrate adhesion plane, and the z axis normal to the substrate (Fig. 1.a,b). Within this coordinate system, CT positions can be expressed using radial (ρ), planar angular (θ), and azimuthal (φ) coordinates. A key requirement for cross-cell comparison is the stability of nuclear orientation. Nuclear rotations in the x–y plane (i.e. around the z-axis) are transmitted coherently to the nucleoplasm and thus to CTs positions[43,47]. In principle, out-of-plane rotations could disrupt a shared φ angular reference, particularly during early stages of cell adhesion, when cells initially contact the surface with variable orientations (Fig. 1.c). To assess whether such rotations occur, we examined nuclear organization and CT positioning during early adhesion.

First, we tested whether early adhesion itself constrains nuclear organization by analyzing hMSCs adhering to fibronectin-coated glass substrates. Three-dimensional renderings of the cellular and nuclear surfaces were obtained from confocal z-stacks of phalloidin- and DAPI-stained hMSCs fixed at different time points (5, 10, 20, 30 minutes, and 16 hours after seeding) (Supplementary Fig. 1.a). Our data showed that cells sharply reduced their height (Supplementary Fig. 1.b) while maintaining a rounded morphology during the earliest stages of adhesion (Supplementary Fig. 1.c) and progressively increasing their projected area (Supplementary Fig. 1.d). Nuclear shape followed the same trend, with nuclei decreasing in height (Supplementary Fig. 1.e), acquiring a more oblate geometry (Supplementary Fig. 1.f) and increasing in nuclear volume (Supplementary Fig. 1.g).

We next examined the radial positioning of CTs across early adhesion stages. We painted chromosome territory 6 (CT6), which is known to occupy a peripheral position in hMSC nuclei[48] (Supplementary Fig. 2.a). Assuming that nuclei undergo substantial out-of-plane reorientation, projection onto the x–y plane would mask radial organization, yielding an apparently random distribution of CT positions (Fig. 1.d). To test this possibility, CT6 centroids were extracted from three-dimensional confocal reconstructions and their radial localization was quantified using normalized distance from the nuclear perimeter (NDNP), defined relative to the x–y projected nuclear boundary (Fig. 1.e). Our analysis showed that CT6 remained localized near the nuclear periphery even during the earliest phases of adhesion and maintain stable radial positioning throughout the adhesion process (Fig. 1.f). Together, the rapid cellular flattening and the stable peripheral positioning of CT6 territories argue against the possibility of out-of-plane nuclear reorientation during the early phase of cell adhesion. These results align with reports indicating that out-of-plane rotation has been observed only in specific cell lines and under specific 3D culture conditions[49–52].

Additionally, we asked whether hMSCs, together with their nuclei, were already polarized during early cell attachment. To address this question, we used Golgi positioning relative to the nucleus, a widely used readout of cellular and nuclear polarity[53,54]. Three-dimensional reconstructions revealed that within minutes of adhesion, when both the cell body and the nucleus remain nearly spherical, the nucleus–Golgi axis was already non-randomly oriented. In fact, our data showed that the nucleus was

preferentially positioned lateral to the Golgi apparatus, resulting in a consistent side-by-side nucleus–Golgi arrangement' (Supplementary Fig. 1.h-k).

Together, these observations indicate that early adhesion rapidly establishes a polarized nuclear configuration, providing a stable reference frame for comparing chromosome positioning across cells thereby supporting the use of a shared coordinate system for subsequent analyses.

2. A 2D nuclear reference frame for comparing nuclear organization

Having established that nuclear orientation is stable and polarity-defined, we next constructed a shared two-dimensional reference frame for cross-cell comparison. At the adhesion steady-state (i.e., after 16 hours of culture), nuclei were aligned by first orienting their major axis along a common direction (parallel to the image y-axis), followed by an in-plane rotation to position the Golgi apparatus consistently relative to the nucleus, a widely used proxy for cellular polarity[43]. This procedure defines a reproducible polarity-registered coordinate system across the cell population (Fig. 2.a).

Direct comparison of chromosome positioning is further complicated by variability in nuclear size, shape, and ellipticity across cells. To account for this, we applied an affine normalization procedure in which each nucleus is approximated as an ellipsoid defined by its principal semi-axes (A, B, C), and spatial coordinates are rescaled accordingly (Fig. 2.b,c). This transformation maps each nucleus onto a unit sphere, enabling geometry-independent comparison of spatial organization, as proposed in recent normalization-based approaches[55]. In this normalized reference frame, the angular distribution of Golgi centroids across the population is bimodal. Kernel density estimation (KDE) revealed two distinct polarity configurations, termed Side and Top (Fig. 2.d), occupying separate angular sectors (Side: 135°–225°; Top: 226°–315°). These configurations define recurrent polarity states within the hMSC population and are consistent with previous observations linking Golgi positioning to cell polarity and directional organization[43].

To assess how CT positioning relates to these polarity states, we analyzed chromosome territories 6 (CT6) together with chromosome territories 12 (CT12), which occupy peripheral-intermediate nuclear regions[37,55] (Fig. 2e). Mapping CT centroids in both laboratory and normalized coordinates showed that chromosome positioning is largely confined to the x–y plane, with minimal contribution from the out-of-plane dimension (Supplementary Fig. 3). Accordingly, subsequent analyses were restricted to a two-dimensional representation.

Importantly, affine normalization preserves key spatial relationships. Radial distributions remain unchanged (Supplementary Fig. 4.a), while angular distributions become more homogeneous across cells (Supplementary Fig. 4.b), in agreement with previous normalization-based analyses[55]. Measures of inter-homolog distance (ID) and interphysical distance (IPD) are also preserved (Supplementary Fig. 4.c,d), and the transformation is invertible, allowing reconstruction of standardized nuclear geometries (Supplementary Fig. 4.e).

Classification of nuclei based on Golgi-defined polarity revealed that Side and Top states are associated with distinct spatial probability maps for both CT6 and CT12 (Fig. 2.f), despite their overall peripheral localization.

Taken together, these findings establish a polarity-registered and geometrically normalized reference frame that enables quantitative comparison of chromosome positioning across heterogeneous nuclei. Within this framework, recurrent polarity states emerge as distinct organizational contexts associated with specific spatial distributions of CTs.

3. Homolog-specific classification reveals polarity-dependent chromosomal positioning

Population-level chromosome maps are typically computed by pooling homologous chromosomes, an approach that can obscure structured spatial organization within diploid nuclei. To resolve this limitation, we sought to identify and track homologous chromosome territories across cells, enabling homolog-resolved spatial analysis.

To this end, we implemented a similarity-based classification algorithm to assign homolog identities across the population (i.e., *Side* and *Top polarity states*). The algorithm operates on CT coordinates expressed in the normalized nuclear reference frame described above (see Methods and Supplementary Files). For each nucleus, both CT6 and CT12 homologs were jointly considered, forming a four-chromosome configuration. When comparing two nuclei, all possible homolog assignments were evaluated, and the configuration minimizing the total Euclidean distance between corresponding CT centroids was selected (Fig. 3.a). By iteratively linking the most similar configurations across the dataset, the algorithm reconstructs a globally consistent homolog labeling, analogous to approaches used for tracking structurally similar configurations across populations.

Homolog classification revealed that, for both CT6 (Fig. 3.b) and CT12 (Fig. 3.c), the two homologous territories (α and β) occupy distinct and reproducible spatial regions within the nuclear reference frame (Supplementary Fig. 5). Notably, nuclear polarity differentially affects the positioning of the two homologs. For CT6, one homolog (CT6α) occupies a consistent spatial region across both Side and Top hMSC polarity states, whereas the second homolog (CT6β) undergoes polarity-dependent repositioning, shifting across angular sectors (Fig. 3.b). A similar pattern was observed for CT12. CT12α retains a stable peripheral distribution with a characteristic bilobed organization, while CT12β displays a polarity-dependent radial shift toward more internal nuclear regions in Top nuclei (Fig. 3.c).

These findings indicate that homologous chromosomes do not behave equivalently within the nucleus, but instead exhibit asymmetric spatial organization. Previous studies have reported recurrent homolog arrangements and inter-homolog relationships[56–59], but have generally not resolved homolog identity across populations. Our results extend these observations by demonstrating that homolog-specific positioning is structured, reproducible, and modulated by cellular polarity.

To assess the robustness of homolog-resolved spatial maps, we generated synthetic datasets using two perturbation strategies: (i) independent angular randomization of CT positions (RdmRot), and (ii) rigid-body rotation of entire nuclei (RigidRot), preserving radial distances in both cases (see Materials and Methods). As controls, additional datasets were generated by subsampling the original data (SubSampN40, SubSampN30, SubSampN20). For each condition, spatial maps were reconstructed and compared using a kernel-density-based two-sample test.

Randomization of nuclear orientation resulted in a marked loss of spatial consistency, with a substantially lower proportion of non-significant comparisons relative to subsampled datasets (Supplementary Fig. 6.a). In contrast, subsampling preserved map structure, indicating that the observed spatial patterns are robust to sample size but sensitive to orientation. These results demonstrate that polarity registration is essential for maintaining reproducible chromosome positioning patterns.

Finally, comparisons between Side and Top populations revealed differential stability between homologs. Spatial maps of α homologs showed high similarity across polarity states, whereas β homologs exhibited significant differences (Supplementary Fig. 6.b). This asymmetry highlights the coexistence of polarity-independent and polarity-dependent components of chromosome organization. Collectively, these results show that homolog-resolved mapping reveals structured and polarity-dependent spatial organization of CTs. By resolving homolog identity within a shared coordinate system, this approach uncovers spatial features that remain concealed in pooled analyses and provides evidence for the existence of distinct nuclear topological states.

4. Micropattern-based geometric confinement standardizes Side- and Top-Like cellular architectures

The identification of Side and Top nuclear polarity states suggests that chromosome organization is coupled to cellular polarity and morphology. Indeed, these two populations exhibit distinct cell shapes and cytoskeletal architectures, with Side cells displaying more spread and isotropic morphologies, and Top cells exhibiting more elongated and anisotropic configurations (Fig. 4.a; Supplementary Fig. 7.a). This coupling indicates that cellular geometry and polarity jointly drive to the establishment of nuclear organization, consistent with previous observations linking cell shape and cytoskeletal organization to chromatin architecture[37,55].

To directly test this relationship, we used single-cell micropatterning to impose defined cell geometries and polarity states. Fibronectin-coated adhesive islands with circular or rectangular shapes were designed to constrain hMSCs into rounded or elongated morphologies, respectively (Fig. 4.b). Pattern sizes were selected to match the range of spreading areas observed in unconstrained cells, enabling direct comparison between confined and native conditions (Fig. 4.a).

Geometric confinement reproducibly induced polarity states analogous to those observed in unconstrained cells. Cells confined to circular patterns adopted a Side-Like configuration, characterized by lateral positioning of the Golgi relative to the nucleus. In contrast, cells on rectangular patterns displayed a Top-Like configuration, with a defined nucleus–Golgi axis aligned along the major cellular

axis (Fig. 4.c). These results demonstrate that cellular polarity states can be externally imposed through geometric constraints.

Consistent with these observations, micropatterned confinement also induced distinct cytoskeletal organizations. Side-Like cells exhibited a more isotropic F-actin network without any preferred orientation, whereas Top-Like cells developed aligned actin bundles along the major cellular axis (Supplementary Fig. 7.b,c), reflecting the anisotropic mechanical environment imposed by rectangular confinement. These findings are in agreement with previous studies showing that cell geometry governs cytoskeletal organization and intracellular force distribution[4,44].

We next examined the impact of geometric confinement on nuclear morphology. Side nuclei displayed a more oblate geometry compared to Top nuclei, and these differences were further amplified under confinement. In particular, nuclei in circular patterns exhibited increased flattening, while nuclei in rectangular patterns were more elongated (Supplementary Fig. 8.a-d). Nuclear volume also varied with cell spreading and polarity state, with Side-Like cells exhibiting larger nuclear volumes compared to Top-Like cells (Supplementary Fig. 8.e). Together, these results show that geometric confinement not only imposes defined polarity states but also systematically reorganizes cytoskeletal architecture and nuclear morphology. This provides a controlled experimental framework for investigating how mechanical and polarity cues shape nuclear organization and chromosome positioning.

5. Confinement preserves homolog-specific chromosomal topology and reveals robust nuclear topological classes

Having established that geometric confinement reproducibly imposes defined polarity states, we next asked whether homolog-specific chromosome organization is preserved under these conditions. This provides a stringent test of whether the nuclear topological states identified in unconstrained cells reflect robust organizational features or arise from population variability. Homolog-resolved mapping revealed that, across all confinement conditions, α and β homologs occupy distinct and well-defined spatial regions within the normalized nuclear reference frame (Fig. 5; Supplementary Fig. 9.a). These regions remain homolog-specific and are characterized by reproducible radial and angular distributions (Supplementary Fig. 10.a,b; Supplementary Fig. 11.a,b), indicating that homolog identity is preserved under geometric constraints.

We first examined CT6 organization in Side-Like cells and compared it to unconstrained Side populations. The spatial distribution of CT6α remained largely unchanged, with conserved radial positioning and only minor angular shifts (Fig. 5.b; Supplementary Fig. 9.b, S10.c, S11.c). In contrast, CT6β displayed pronounced reorganization, characterized by a substantial angular displacement (Fig. 5.b; Supplementary Fig. 9.b, S11.c), consistent with its polarity-dependent behavior. We next analyzed CT6 organization in Top-Like cells relative to unconstrained Top populations. As observed for Side conditions, CT6α maintained stable spatial positioning, preserving both radial and angular distributions (Fig. 5.e; Supplementary Fig. 9.b, S10.c, S11.c). Conversely, CT6β exhibited both radial and

angular shifts under confinement, indicating sensitivity to changes in cellular geometry and polarity (Fig. 5.e; Supplementary Fig. 10.c, S11.c).

Similar trends were observed for CT12 territories. In Side-Like cells, CT12α preserved its radial and angular positioning, although its spatial distribution transitioned from a bilobed pattern to a single dominant density region (Fig. 5.c; Supplementary Fig. 9.b, S10.c, S11.c). CT12β showed minimal changes in both radial and angular positioning, maintaining a stable spatial configuration across conditions (Fig. 5.c; Supplementary Fig. 9.b, S10.c, S11.c). In Top-Like cells, CT12α exhibited minor changes in density distribution while preserving overall radial and angular positioning (Fig. 5.f; Supplementary Fig. 9.b, S10.c, S11.c). Similarly, CT12β remained largely unchanged in both spatial distribution and positioning metrics (Fig. 5.f; Supplementary Fig. 9.b, S10.c, S11.c). Consistent with these observations, global spatial descriptors, including inter-homolog distance (ID) and interphysical distance (IPD), remained stable across confined and unconstrained conditions (Supplementary Fig. 12), further supporting the robustness of homolog-specific organization. Collectively, these results demonstrate that geometric confinement preserves key features of homolog-resolved chromosome topology while enabling reproducible control of nuclear polarity states. This consistency across independent experimental conditions supports the existence of robust and reproducible nuclear topological states, defined by specific combinations of polarity, nuclear geometry, and homolog-specific chromosome positioning.

Discussion

The non-random spatial organization of CTs within the interphase nucleus has been established for over than two decades. Early studies established that chromosomes occupy preferential radial positions[9–13] and that homologous chromosomes can adopt recurrent intranuclear arrangements across cells[56,57]. However, systematic identification of such configurations has remained limited by the absence of a shared reference framework, particularly in cells with variable geometry and orientation. More recent work has highlighted the role of cell polarity and cytoskeletal organization in shaping nuclear architecture. In polarized cells, Golgi orientation has been used to define nuclear directionality, revealing asymmetric nuclear organization along polarity axes[43]. In parallel, mechanical cues transmitted through the cytoskeleton have been shown to influence chromatin organization and chromosome positioning[4,26,37]. Together, these studies suggest that nuclear architecture is tightly coupled to cell geometry and mechanical state, yet a quantitative framework enabling rigorous cross-cell comparison has remained lacking. In this work, we address this limitation by introducing a polarity-registered and geometrically normalized coordinate framework that enables homolog-resolved mapping of CTs across cell populations. By aligning nuclei based on intrinsic polarity cues and normalizing nuclear geometry, we transform heterogeneous nuclei into a shared coordinate system that integrates both radial and angular information. This approach extends traditional radial mapping strategies[9,12,48,60] by incorporating polarity registration and homolog resolution into a unified spatial representation.

A central finding of this work is that chromosome organization in adherent cells is not adequately described as a continuous or stochastic distribution. Instead, we show that cell populations can be partitioned into discrete and reproducible nuclear topological states, defined as stable spatial probability distributions of homolog-resolved chromosome territories within a shared coordinate system. Previous studies reported recurrent chromosome arrangements and non-random nuclear organization[56,57], but the absence of a shared spatial reference framework has made it difficult to distinguish structured configurations from rotational or geometric variability. More recent approaches based on radial positioning or population-averaged measurements[9,12,48,60] have further supported non-random organization but remain limited in resolving angular and polarity-dependent structure. These limitations have hindered the identification of higher-order spatial organization across cell populations. By explicitly accounting for nuclear orientation and geometry, our framework reveals structured spatial heterogeneity that would otherwise be masked in conventional analyses. Homolog-resolved analysis further reveals asymmetric spatial behavior between chromosome copies. While one homolog consistently occupies a stable spatial niche, the other displays polarity-dependent repositioning. This structured asymmetry suggests that homolog-specific plasticity may represent a general feature of diploid nuclear organization rather than stochastic variability. Previous studies have reported recurrent homolog arrangements and inter-homolog relationships[56–59], but these have largely been analyzed without resolving homolog identity at the population level. Our results extend these observations by demonstrating that homolog asymmetry is structured, reproducible, and coupled to cellular polarity. Importantly, micropattern-based geometric confinement[44–46] demonstrates that these nuclear topological classes can be experimentally stabilized. By imposing defined cell geometries and polarity axes, we obtain coherent and homogeneous nuclear configurations across populations, indicating that nuclear topology is not merely an emergent property but can be systematically controlled through mechanical and polarity constraints. This finding aligns with previous reports showing that cell geometry and cytoskeletal organization influence chromatin organization and gene expression[4,4,26], and extends them by demonstrating that mechanical constraints can stabilize discrete nuclear topological configurations.

These findings have broader implications for spatial genomics and 3D genome mapping. Contact-based approaches such as Hi-C and related assays quantify interaction frequencies but do not directly encode spatial positioning within a polarity-registered coordinate system. If cell populations are composed of multiple discrete topological classes, population-averaged contact maps may mask structured spatial heterogeneity. This limitation has been increasingly recognized in studies highlighting cell-to-cell variability in genome organization[61,62]. By providing homolog-resolved spatial probability maps within a shared coordinate framework, our approach offers a complementary strategy for integrating imaging-based measurements with population-level genomic data.

Several limitations should be considered. This study focuses on a limited set of CTs in a polarity-constrained adherent cell type, and extension to additional chromosomes and cellular contexts will be required to assess the generality of the observed topological classes. Moreover, while the homolog assignment algorithm is computationally tractable at the current scale, further optimization may be

needed for application to highly multiplexed datasets. Finally, in systems where nuclear orientation cannot be reliably registered, such as suspended cells or cells with pronounced nuclear dysmorphia, adaptations of the framework will be necessary.

In summary, by integrating polarity registration, geometric normalization, and homolog-resolved mapping, we provide a quantitative framework for classifying nuclear organization into discrete topological states. This work builds on and unifies prior observations of non-random chromosome positioning and polarity-dependent nuclear organization[9,12,43,48], and extends them by demonstrating that nuclear architecture can be partitioned into reproducible topological states. More broadly, this framework reconciles structured chromosome positioning with single-cell variability and establishes a methodological foundation for comparative analyses of nuclear architecture across mechanical, developmental, and pathological contexts. As spatially resolved genomic technologies continue to expand, the ability to compare nuclear organization within a shared coordinate system will be essential for distinguishing stochastic variability from structured spatial organization.

Materials and Methods

Cell culture

Human bone marrow–derived mesenchymal stem cells (hMSCs; Lonza, PT-2501) in passages 5 to 6 were cultured in α-MEM (Euroclone) supplemented with 10% fetal bovine serum (FBS), 1% L-glutamine and 1% penicillin–streptomycin at 37°C and 5% CO_2. After 4 days of culturing, cells were detached with trypsin for 5 min and seeded on untreated and patterned substrates at a density of 4000 cells/cm^2.

Cell fixation and immunostaining

hMSCs were fixed at different time points in 4% paraformaldehyde (PFA) in PBS for 20 min at room temperature, rinsed in PBS, and stored at 4°C until processing. The cells were permeabilized with 0.1% Triton X-100 (15 min), blocked with 3% BSA in 0.1% Triton-PBS (1 h), and incubated with anti-giantin primary antibody (overnight, 4°C) followed by fluorophore-conjugated secondary antibodies (1 h, room temperature). F-actin was stained with phalloidin (1 h) and nuclei were counterstained with DAPI (15 min). Samples were mounted in Vectashield™ and stored at 4°C.

Chromosome painting

Chromosome painting was performed using a fluorescence in situ hybridization (FISH) protocol adapted from[55,63]. The Golgi apparatus was immunolabeled first and samples were post-fixed as above. Prior to hybridization, samples were incubated in 20% glycerol/PBS (1 h, room temperature), 50% glycerol/PBS (24 h, – 20°C), then 20% glycerol/PBS (1 h, room temperature), followed by three rapid immersions in liquid nitrogen. Cells were permeabilized in 0.07% Triton X-100/0.1 M HCl (5 min) and denatured in 50%

formamide/2× SSC (10 min, room temperature). Then, chromosome painting probes for chromosomes 6 and 12 (MetaSystems XCyting Chromosome Paints) were added to the specimen, denatured for 3 min at 75°C, and hybridized overnight at 37°C. Post-hybridization washes were performed in 2× SSC and 0.1× SSC (10 min each at 45°C). Nuclei were counterstained with DAPI and samples were mounted in Vectashield™ and stored at − 20°C.

Single cell micropatterning

Culture substrates featuring microscopic single-cell adhesive islands were fabricated using a deep-UV micropatterning technique, following the protocol described by Azioune et al.[64]. Circular and rectangular substrates with areas of 5,000 and 1,500 μm², respectively, were fabricated. Glass coverslips were first activated by exposure to O_2 plasma for 1 min and incubated for 1 h with PLL-g-PEG (0.1 mg/ml in 10 mM HEPES) for passivation. After rinsing with distilled water, the treated surfaces were exposed to deep UV irradiation for 5 min through a chromium-on-quartz photomask (4DCell) bearing the desired micropattern geometry, in order to selectively ablate the targeted PLL-g-PEG regions. Unconfined counterparts were obtained by full UV exposure. Prior to cell seeding, all patterned and reference substrates were incubated for 1 h with 50 μg/mL fibronectin solution at room temperature, followed by two washes in 1x PBS.

Confocal imaging

Confocal imaging was performed on a Zeiss LSM 900 microscope using a 63× oil-immersion objective. Multichannel z-stacks were acquired at 512 × 512 pixels with a z-step of 0.22 μm and saved as 16-bit image stacks. Only isolated, well-spread cells fully occupying the adhesive island were imaged. Acquisition settings were kept constant across samples within each imaging mode.

Image Analysis

Cell and nuclear registration

Depending on the imaging mode, either chromosome-painted nuclei or single whole-cells were isolated and placed on a uniform square canvas. Images were registered using rigid in-plane transformations only (translation and rotation; no scaling or reflection). For chromosome-painted datasets, nuclei were centered based on the DAPI signal, aligned by their major axis. They were subsequently oriented such that the Golgi centroid lay within the 135°–315° angular sector relative to the nuclear centroid. For unconfined cells, centering and alignment were based on the actin contour and its major axis, and final orientation was set by Golgi position using the same conventions as the corresponding chromosome-painted nuclei. For rectangular micropatterns, the centroid of the actin-defined cell contour was translated to the image center and the cell was rotated to align its longitudinal axis. Orientation was standardized to reproduce the imposed front–rear polarity, with the nucleus positioned at the top and the Golgi at the bottom of the image. For circular micropatterns, images were centered using the circular cell

contour, aligned by the major nuclear axis, and oriented so that the Golgi consistently lay on the left of the nucleus. All registration steps were performed in ImageJ (NIH) using custom macros.

3D reconstruction

Three-dimensional reconstructions and quantitative analyses were performed in Imaris 10.0 (Oxford Instruments) using the Surfaces module. Pre-processed and registered z-stacks from ImageJ were imported into Imaris and segmented into 3D surfaces.

For whole-cell datasets (actin/Golgi/DAPI), surfaces were generated for the cell body (actin), nucleus (DAPI), and Golgi apparatus. Morphometric descriptors (including volume, ellipsoidal descriptors, semi-axis lengths and centroid coordinates) and fluorescence intensity statistics were extracted for each compartment.

For chromosome-painting datasets (DAPI/Golgi/CT6/CT12), the nuclear surface was reconstructed from DAPI and CTs were segmented from the corresponding channels. When homologous territories were contiguous, they were separated using the Morphological Split function.

Cell adhesion classification

Since early cell adhesion is an asynchronous process within a cell population, adhesion stages were assigned based on cell morphology rather than nominal fixation time. For each cell, projected cell area was measured in ImageJ, and cell height was extracted in Imaris software. The two features were clustered using k-means clustering (k = 5) performed in R, yielding five morphology-defined adhesion time classes. Subsequent analyses (chromosome radial positioning and nucleus–Golgi orientation classification) were performed within these classes.

3D nucleus-Golgi orientation

The relative 3D arrangement of nucleus and Golgi was classified into three categories (basal, lateral or apical) using three independent criteria applied to each cell.

1. (i) *Visual scoring.* Classes were assigned by visual inspection of 3D reconstructions.
2. (ii) *Centroid-overlap criterion.* The z-intervals occupied by nucleus and Golgi were defined from their centroid positions and respective object heights. Configurations with ≥50% overlap of these intervals were classified as lateral. For < 50% overlap, configurations were classified as apical when the Golgi centroid was above the nuclear centroid and as basal when it was below.
3. (iii) *Angular criterion.* The angle φ between the z-axis (the positive z-axis was defined as the apical direction) and the vector connecting the nuclear and Golgi centroids was computed as

$$\phi = \arccos\left(\frac{\Delta z}{\sqrt{(\Delta x)^2 + (\Delta y)^2 + (\Delta z)^2}}\right)$$

and cells were classified as Apical (0°≤φ ≤ 60°), Lateral (60° < φ ≤ 120°) or Basal (120° < φ ≤ 180°). For each cell, the final label was defined by majority vote across the three criteria.

Coordinate normalization

Each registered nucleus was approximated as an ellipsoid defined by its semi-axes (A < B < C) and centered at the nuclear centroid. Chromosome-territory centroid coordinates (X, Y, Z), expressed in the nuclear principal-axis frame, were normalized by axis-wise scaling:

$$X_{circ} = \frac{X}{B}, Y_{circ} = \frac{Y}{C}, Z_{circ} = \frac{Z}{A}$$

This affine transformation maps the nuclear ellipsoid to a unit sphere. For 2D analyses, normalized coordinates were projected onto the x-y plane. Cartesian coordinates were also converted to spherical coordinates both in the nuclear reference frame (X, Y, Z) and after normalization (x, y, z):

$$\rho = \sqrt{x^2 + y^2 + z^2}$$

$$\theta = atan2\left(x, y\right)$$

$$\phi = arccos\left(\frac{z}{\rho}\right)$$

With $\theta \in (-\pi, \pi]$ (azimuth in the x-y plane) and $\phi \in [0, \pi]$ (polar angle from the $+Z$ axis).

Homolog classification algorithm

To assign homolog identities consistently across the entire population, we implemented a labeling algorithm based on configuration similarity between nuclei. Each nucleus is represented by the set of centroid coordinates of all CTs considered (here, both homologs of chromosomes 6 and 12). Pairwise similarity between two nuclei is quantified by the sum of squared Euclidean displacements required to superimpose corresponding chromosome-territory centroids. Because homologs are initially indistinguishable, the distance is evaluated for all possible within-chromosome homolog matchings and the minimum value is retained, corresponding to the most efficient assignment between the two nuclei. Starting from a chosen reference nucleus, the algorithm iteratively identifies the most similar nucleus among those not yet visited, and propagates homolog labels along this ordered sequence, effectively producing a “tracking” of homolog identities across nuclei. Each ordered sequence (path) has an associated global cost (energy), defined as the sum of squared centroid displacements between consecutive nuclei. The procedure is repeated using each nucleus as starting reference, and the path with minimal total energy is selected to define the final population-wide homolog labeling. The algorithm was implemented in R; detailed pseudocode is provided in Supplementary Methods. We clarify that, homolog classes were coherently renamed a posteriori, designating the spatially stable homolog as α and the polarity-responsive one as β. This nomenclature is purely descriptive and does not affect the underlying classification.

Kernel density estimation and spatial probability maps

To visualize population-level spatial distributions of CT centroids, we computed bivariate kernel density estimates (KDEs) from 2D projections of the 3D coordinates onto the principal planes (x-y, x-z and y-z) in the nuclear reference system and in the normalized reference system:

$$\widehat{f}(x;H) = \frac{1}{n}\sum\nolimits_{i=1}^{n} K_H(x - X_i)$$

where $K_H$is a symmetric Gaussian kernel function scaled by the bandwidth matrix *H.* KDEs were computed in R using the 'ks' package[65] and the optimal *H* was estimated using the default algorithm. Density fields were visualized as contour maps at cumulative density levels of 25%, 50%, 75% and 100%.

Chromosomal maps stability analysis

To assess the robustness of the chromosomal maps, we performed a stability analysis using synthetic datasets generated from the original observations.

To evaluate the effect of nuclear orientation in the x-y plane, two strategies were used to generate synthetic datasets. In the first strategy, each CT was independently assigned a random angle θ in the x-y plane, simulating independent random rotations (RdmRot) of chromosome positions. In the second strategy, all CTs within the same nucleus were rotated by the same random angular displacement, simulating rigid-body rotation (RigidRot) of the entire nucleus. In both approaches, the radial distance of each CT from the nuclear center was preserved.

To assess the effect of sample size, three additional sets of synthetic datasets were generated by random subsampling of the original observations, yielding datasets containing 40 (SubSampN40), 30 (SubSampN30), or 20 (SubSampN20) observations.

For each perturbation strategy, 10 independent synthetic datasets were generated. Hence, chromosomal maps were reconstructed for each dataset using the same pipeline applied to the original data. For each perturbation strategy, all synthetic datasets were compared to each other and to the original dataset. Map similarity was assessed using a kernel-density-based two-sample comparison test ("kde.test" function from the 'ks' R package). Robustness was summarized as the percentage of non-significant comparisons, calculated as:

$$ns\ \% = \frac{[number\ of\ pairwise\ comparisons\ with\ p\ \geq\ 0.05]}{[total\ number\ of\ pairwise\ comparisons\ ]} * 100$$

Normalized distance from the nuclear perimeter

For each CT, we computed the distance to the nuclear boundary (in the x-y plane) along the radial direction connecting the nuclear centroid to the CT centroid. In the cartesian nuclear reference frame CT

radial distance from the nuclear centroid was defined as R_{CT} (Euclidean distance). The corresponding radial distance from the nuclear centroid to the nuclear perimeter along the same direction was defined as R_{NP} and obtained by intersecting the centroid–CT ray with the nuclear contour (perimeter extracted from the nuclear mask in ImageJ). The normalized radial position was then computed as:

$$r = \frac{R_{CT}}{R_{NP}}$$

and the normalized membrane distance as:

$$NDNP = \delta = \frac{R_{NP} - R_{CT}}{R_{NP}} = 1 - r$$

In the normalized (unit-circle) reference system, the same parameters were computed directly as:

$$r_{circ} = \sqrt{\left(X_{circ}^2 + Y_{circ}^2\right)}$$

$$NDNP = \delta_{circ} = 1 - r_{circ}$$

Inter-homolog Distance

To assess the proximity between homologous CTs, the Euclidean inter-distance between the centroids of the two copies (CT_α and CT_β) of the CT pair j (either 6 or 12) in each single nucleus was computed in the x-y plane as:

$$ID_j = \sqrt{(x_{CT_\alpha^j} - x_{CT_\beta^j})^2 + (y_{CT_\alpha^j} - y_{CT_\beta^j})^2}$$

Interphysical Distance

The interphysical distance (IPD), which captures the average spatial distance between all possible homolog-specific CT centroids pairs from different chromosomes in each single nucleus[59], is defined (for *N* chromosomes) as:

$$IPD = \frac{1}{N^2} \sum_{i \in \{\alpha, \beta\}} \sum_{j \in \{\alpha, \beta\}} d_{CT_i^6,\, CT_j^{12}}$$

where *d* represents the Euclidean distance between homolog-specific CT centroids pairs. In the present study, *N = 2* (chromosomes 6 and 12), yielding:

$$IPD = \frac{1}{4}(d_{CT_\alpha^6,\, CT_\alpha^{12}} + d_{CT_\alpha^6,\, CT_\beta^{12}} + d_{CT_\beta^6,\, CT_\alpha^{12}} + d_{CT_\beta^6,\, CT_\beta^{12}})$$

Actin cytoskeleton characterization

Registered z-stacks were processed in ImageJ. The actin channel was isolated and projected onto the x-y plane using a sum-intensity projection across the full cell z-range. Cells were segmented from the actin projection to extract morphological descriptors (projected area, aspect ratio and ellipticity) and actin intensity statistics (mean, minimum, maximum and standard deviation). Fiber alignment was quantified using OrientationJ (ImageJ) by computing the dominant orientation and coherency for each cell. For population-level actin maps, single-cell actin projections from the same experimental condition were overlaid and summed to generate actin density maps.

Statistical analysis

All statistical analyses were performed in R. Comparisons of 1D variables (i.e., all *non-angular* descriptors, including radial or distance-like metrics such as NDNP / radial coordinate, ID, IPD) were carried out using pairwise Wilcoxon tests. Comparisons of angular variables (e.g., in-plane angles θ) were performed using pairwise Watson–Wheeler tests for homogeneity of circular distributions.

Population-level spatial probability maps estimated by KDE were compared using a kernel-density–based global two-sample comparison test on the resulting 2D distributions. For these comparisons, we focused specifically on the high-density regions defined by the first three KDE quartiles (25%, 50%, 75% cumulative-density contours). Low-density tails, reflecting biological variability, were retained for visualization but excluded from quantitative comparisons. For analyses involving multiple pairwise comparisons, *P* values were adjusted using the Bonferroni correction. Significance was annotated as: ns ($P \geq 0.05$), * ($P < 0.05$), ** ($P < 0.01$), *** ($P < 0.001$), **** ($P < 0.0001$). At least n = 15 cells/nuclei were acquired per condition in each of three independent experiments.

Declarations

Data availability

The dataset is available from the corresponding author upon reasonable request.

Code availability

The custom code developed for homolog classification is available in the supplementary information. All other code used in the analysis are available upon request to the corresponding authors.

Competing Interest Statement:

The authors declare no competing interests.

Author Contributions:

P.A.N. conceived the study and directed the project. L.M. performed the experiments, developed the computational algorithm, carried out image processing and data analysis, and generated the results. C.F.N. supervised the study and contributed to data interpretation. L.M., C.F.N., and P.A.N. wrote, reviewed, and edited the manuscript.

References

1. Schoenfelder S, Fraser P (2019) Long-range enhancer–promoter contacts in gene expression control. Nat Rev Genet 20:437–455
2. Marchal C, Sima J, Gilbert DM (2019) Control of DNA replication timing in the 3D genome. Nat Rev Mol Cell Biol 20:721–737
3. Arnould C et al (2023) Chromatin compartmentalization regulates the response to DNA damage. Nature 623:183–192
4. Uhler C, Shivashankar GV (2017) Regulation of genome organization and gene expression by nuclear mechanotransduction. Nat Rev Mol Cell Biol 18:717–727
5. Zheng H, Xie W (2019) The role of 3D genome organization in development and cell differentiation. Nat Rev Mol Cell Biol 20:535–550
6. Cremer T, Cremer M (2010) Chromosome Territories. Cold Spring Harb Perspect Biol 2:a003889–a003889
7. Cremer T, Cremer C (2001) Chromosome territories, nuclear architecture and gene regulation in mammalian cells. Nat Rev Genet 2:292–301
8. Bonev B, Cavalli G (2016) Organization and function of the 3D genome. Nat Rev Genet 17:661–678
9. Bolzer A et al (2005) Three-Dimensional Maps of All Chromosomes in Human Male Fibroblast Nuclei and Prometaphase Rosettes. PLoS Biol 3:e157
10. Bouwman BA, Crosetto N, Bienko M (2023) A GC-centered view of 3D genome organization. Curr Opin Genet Dev 78:102020
11. Bickmore WA, van Steensel B (2013) Genome Architecture: Domain Organization of Interphase Chromosomes. Cell 152:1270–1284
12. Cremer M et al (2001) Non-random radial higher-order chromatin arrangements in nuclei of diploid human cells. Chromosome Res 9:541–567
13. Crosetto N, Bienko M (2020) Radial Organization in the Mammalian Nucleus. Front Genet 11:33
14. Kempfer R, Pombo A (2020) Methods for mapping 3D chromosome architecture. Nat Rev Genet 21:207–226
15. Bouwman BAM, Crosetto N, Bienko M (2022) The era of 3D and spatial genomics. Trends Genet 38:1062–1075
16. Jerkovic´ I, Cavalli G (2021) Understanding 3D genome organization by multidisciplinary methods. Nat Rev Mol Cell Biol 22:511–528

17. Croft JA et al (1999) Differences in the Localization and Morphology of Chromosomes in the Human Nucleus. J Cell Biol 145:1119–1131
18. Nir G et al (2018) Walking along chromosomes with super-resolution imaging, contact maps, and integrative modeling. PLoS Genet 14:e1007872
19. Yang L et al (2023) (Tn5-)FISH-based imaging in the era of 3D/spatial genomics. Biophys Rep 9:15–25
20. Han J, Zhang Z, Wang K (2018) 3C and 3C-based techniques: the powerful tools for spatial genome organization deciphering. Mol Cytogenet 11:21
21. Lieberman-Aiden E et al (2009) Comprehensive Mapping of Long-Range Interactions Reveals Folding Principles of the Human Genome. Science 326:289–293
22. Davies JOJ, Oudelaar AM, Higgs DR, Hughes JR (2017) How best to identify chromosomal interactions: a comparison of approaches. Nat Methods 14:125–134
23. Akgol Oksuz B et al (2021) Systematic evaluation of chromosome conformation capture assays. Nat Methods 18:1046–1055
24. Girelli G et al (2020) GPSeq reveals the radial organization of chromatin in the cell nucleus. Nat Biotechnol 38:1184–1193
25. Finn EH, Misteli T (2019) Molecular basis and biological function of variability in spatial genome organization. Science 365:eaaw9498
26. Tajik A et al (2016) Transcription upregulation via force-induced direct stretching of chromatin. Nat Mater 15:1287–1296
27. Miroshnikova YA, Wickström SA (2022) Mechanical Forces in Nuclear Organization. Cold Spring Harb Perspect Biol 14:a039685
28. Trappmann B et al (2012) Extracellular-matrix tethering regulates stem-cell fate. Nat Mater 11:642–649
29. Lv H et al (2017) Biomaterial stiffness determines stem cell fate. Life Sci 178:42–48
30. Neelam S et al (2015) Direct force probe reveals the mechanics of nuclear homeostasis in the mammalian cell. *Proceedings of the National Academy of Sciences* 112, 5720–5725
31. Watt FM, Huck WTS (2013) Role of the extracellular matrix in regulating stem cell fate. Nat Rev Mol Cell Biol 14:467–473
32. Takaki T et al (2017) Actomyosin drives cancer cell nuclear dysmorphia and threatens genome stability. Nat Commun 8:16013
33. Roy B et al (2018) Laterally confined growth of cells induces nuclear reprogramming in the absence of exogenous biochemical factors. *Proceedings of the National Academy of Sciences* 115, E4741–E4750
34. Natale CF, Ventre M, Netti PA (2014) Tuning the material-cytoskeleton crosstalk via nanoconfinement of focal adhesions. Biomaterials 35:2743–2751

35. Jahed Z, Mofrad MR (2019) The nucleus feels the force, LINCed in or not! Curr Opin Cell Biol 58:114–119
36. Khatau SB et al (2009) A perinuclear actin cap regulates nuclear shape. *Proceedings of the National Academy of Sciences* 106, 19017–19022
37. Wang Y, Nagarajan M, Uhler C, Shivashankar GV (2017) Orientation and repositioning of chromosomes correlate with cell geometry–dependent gene expression. Mol Biol Cell 28:1997–2009
38. Heo S-J et al (2016) Mechanically Induced Chromatin Condensation Requires Cellular Contractility in Mesenchymal Stem Cells. Biophys J 111:864–874
39. Uhler C, Shivashankar GV (2017) Chromosome Intermingling: Mechanical Hotspots for Genome Regulation. Trends Cell Biol 27:810–819
40. Bornens M (2008) Organelle positioning and cell polarity. Nat Rev Mol Cell Biol 9:874–886
41. Luxton GG, Gundersen GG (2011) Orientation and function of the nuclear–centrosomal axis during cell migration. Curr Opin Cell Biol 23:579–588
42. Viana MP et al (2023) Integrated intracellular organization and its variations in human iPS cells. Nature 613:345–354
43. Nastały P et al (2020) Role of the nuclear membrane protein Emerin in front-rear polarity of the nucleus. Nat Commun 11:2122
44. Théry M et al (2006) Anisotropy of cell adhesive microenvironment governs cell internal organization and orientation of polarity. Proc Natl Acad Sci U S A 103:19771–19776
45. Pouthas F et al (2008) In migrating cells, the Golgi complex and the position of the centrosome depend on geometrical constraints of the substratum. J Cell Sci 121:2406–2414
46. Chen B, Kumar G, Co CC, Ho C-C (2013) Geometric Control of Cell Migration. Sci Rep 3:2827
47. Kim D-H, Cho S, Wirtz D (2014) Tight coupling between nucleus and cell migration through the perinuclear actin cap. J Cell Sci 127:2528–2541
48. Parada LA, McQueen PG, Misteli T (2004) Tissue-specific spatial organization of genomes. Genome Biol 5:R44
49. May D et al (2023) Live imaging reveals chromatin compaction transitions and dynamic transcriptional bursting during stem cell differentiation in vivo. *eLife* 12, e83444
50. Nagamatsu G, Shimamoto S, Hamazaki N, Nishimura Y, Hayashi K (2019) Mechanical stress accompanied with nuclear rotation is involved in the dormant state of mouse oocytes. Sci Adv 5:eaav9960
51. Wu YK, Umeshima H, Kurisu J, Kengaku M (2018) Nesprins and opposing microtubule motors generate a point force that drives directional nuclear motion in migrating neurons. Development 145:dev158782
52. Wilson MH, Holzbaur EL (2012) F. Opposing microtubule motors drive robust nuclear dynamics in developing muscle cells. J Cell Sci 125:4158–4169

53. Ravichandran Y, Goud B, Manneville J-B (2020) The Golgi apparatus and cell polarity: Roles of the cytoskeleton, the Golgi matrix, and Golgi membranes. Curr Opin Cell Biol 62:104–113
54. Khuntia P, Rawal S, Marwaha R, Das T (2022) Actin-driven Golgi apparatus dispersal during collective migration of epithelial cells. *Proceedings of the National Academy of Sciences* 119, e2204808119
55. Natale CF et al Material-Induced Nuclear Deformation Controls Chromatin Architecture in Adipose Stem Cells. *Advanced Science* n/a, e14458
56. Nagele RG et al (1999) Chromosomes exhibit preferential positioning in nuclei of quiescent human cells. J Cell Sci 112:525–535
57. Koss LG (1998) Characteristics of chromosomes in polarized normal human bronchial cells provide a blueprint for nuclear organization. Cytogenet Cell Genet 82:230–237
58. Heride C et al (2010) Distance between homologous chromosomes results from chromosome positioning constraints. J Cell Sci 123:4063–4075
59. Iyer KV et al (2012) Modeling and Experimental Methods to Probe the Link between Global Transcription and Spatial Organization of Chromosomes. PLoS ONE 7:e46628
60. Sengupta K et al (2007) Artificially Introduced Aneuploid Chromosomes Assume a Conserved Position in Colon Cancer Cells. PLoS ONE 2:e199
61. Nagano T et al (2013) Single-cell Hi-C reveals cell-to-cell variability in chromosome structure. Nature 502:59–64
62. Stevens TJ et al (2017) 3D structures of individual mammalian genomes studied by single-cell Hi-C. Nature 544:59–64
63. Nastały P, Maiuri P (2021) Preparing Map of Chromosome Territory Distribution Frequency. In: Bodega B, Lanzuolo C (eds) Capturing Chromosome Conformation: Methods and Protocols. Springer US, New York, NY, pp 213–219. doi:10.1007/978-1-0716-0664-3_12.
64. Azioune A, Carpi N, Tseng Q, Théry M, Piel M (2010) Protein micropatterns: A direct printing protocol using deep UVs. Methods Cell Biol 97:133–146
65. Schauer K, Duong T, Bleakley K, Bardin S, Et A (2010) Probabilistic density maps to study global endomembrane organization. Nat Methods. https://doi.org/10.1038/nmeth.1462

Figures

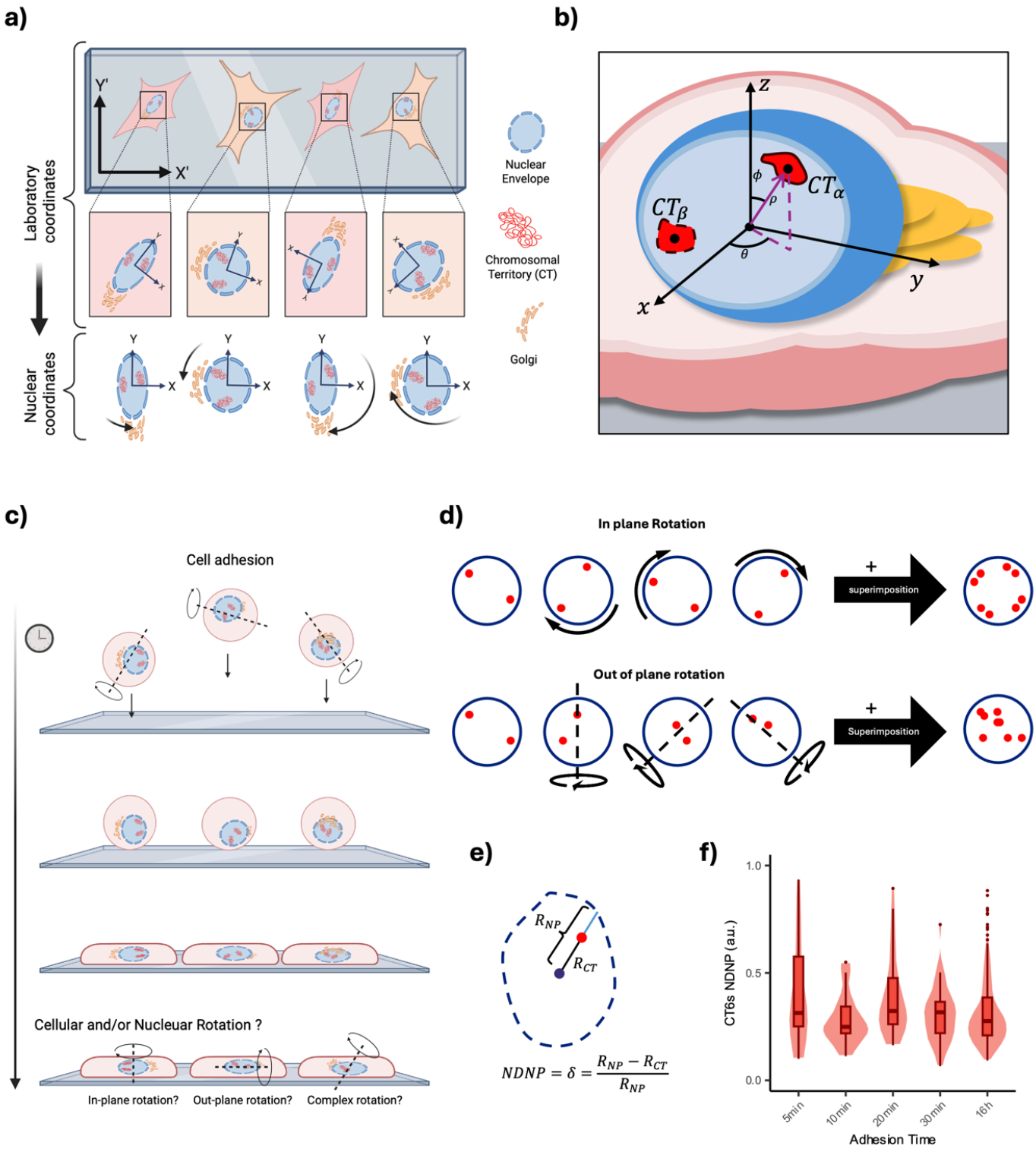


Figure 1

Stable nuclear reference frame during adhesion. (a) Schematic workflow for registering nuclei in a common nuclear reference frame. Created with BioRender.com (b) The coordinate system is defined by the origin at the nuclear centroid; the x–y plane is parallel to the adhesion substrate, and the z axis is perpendicular to it. The spatial position of the two CT homologs CTα (solid contour) and CTβ (dashed contour) is described by the radial coordinate (ρ), planar angle (θ), and azimuthal angle (f). (c) Cartoon

illustrating hypothetical nuclear orientation dynamics during early cell adhesion. As cells transition from suspension to substrate adhesion and spreading, nuclear orientation may undergo distinct rotational regimes, including in-plane, out-of-plane, or multi-axis rotations, potentially introducing stochastic variability in CT positioning across the cell population. Created with BioRender.com (d) Two hypothetical models of nuclear rotational constraints and radial chromosome positioning. (Top row) If nuclear rotation is restricted to in-plane rotations around the substrate-normal axis, chromosomes occupying peripheral niches (e.g., CT6) retain stable radial localization across independently sampled nuclei. (Bottom row) If nuclei rotate around multiple axes, the projected radial distribution of CTs appears randomized across the population. (e) Schematic representation of the NDNP calculation. (f) Distribution of CT6 NDNP across progressive adhesion time points. n ≥ 20 cells for each condition. Statistical significance was assessed using the Kruskal–Wallis test followed by Dunn's multiple-comparison test.

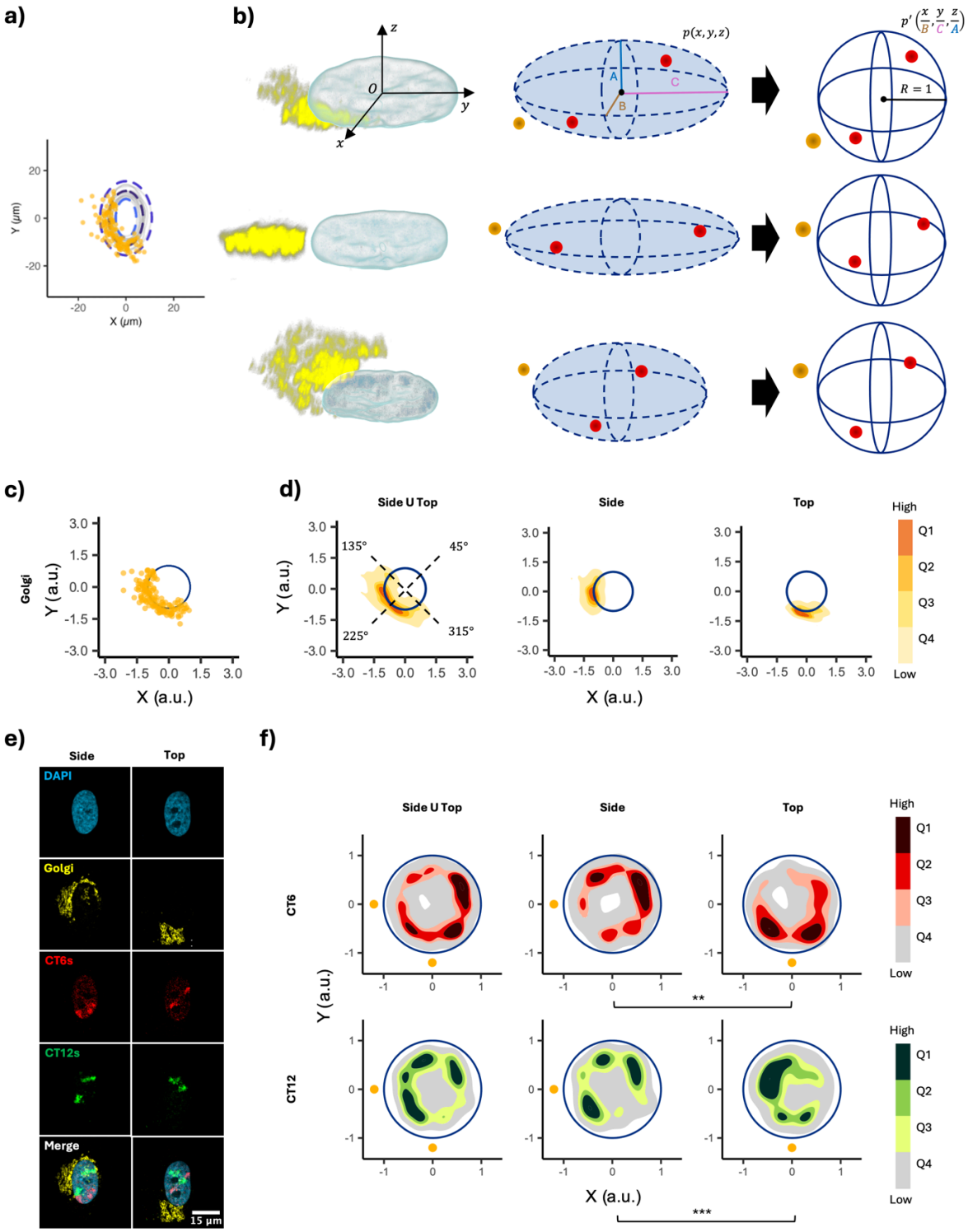


Figure 2

Golgi-oriented nuclear alignment reveals distinct chromosomal topologies. (a) Scatter plot of Golgi centroid positions projected onto the x–y plane in laboratory coordinates (yellow). Gray contours correspond to nuclear perimeters extracted from individual cells in the dataset, with each dashed curve representing a single nucleus. Blue dashed ellipses indicate fitted nuclear profiles corresponding to the smallest, median, and largest nuclear cross-sections. (b) Schematic representation of the coordinate

transformation applied to chromosome territories (red and green) and Golgi (yellow) centroid positions. In the laboratory reference frame (left), nuclear morphology is approximated as an ellipsoid defined by its principal semi-axes (A < B < C) (center). Centroid coordinates $p(x, y, z)$ are normalized by axis-specific rescaling, yielding transformed coordinates p'(x/B, y/C, z/A). This affine transformation maps the ellipsoidal nucleus onto a spherical reference frame (right), enabling geometry-independent spatial comparison. (c) Golgi centroid positions (yellow) projected onto the x–y plane after affine normalization to the unit reference circle (blue contour). Nuclear orientation was standardized such that Golgi centroids localize within the 135°–315° angular sector in circular coordinates. (d) (Left) Kernel density estimation (KDE) map of Golgi centroid positions in the normalized x–y reference frame for the entire population. Shaded contours represent cumulative density quartiles (Q1–Q4). Dashed lines delimit the four angular sectors used for polarity classification. (Center) KDE map of the "Side" subpopulation, defined by Golgi localization within the 135°–225° angular sector. (Right) KDE map of the "Top" subpopulation, defined by Golgi localization within the 226°–315° angular sector. (e) Representative confocal images of hMSCs showing interphase nuclei classified as Side (left) and Top (right). From top to bottom: nucleus (DAPI, blue), Golgi apparatus (anti-giantin, yellow), CT6 (red), CT12 (green), and merged channels. Scale bar, 15 μm. (f) KDE maps of CT6 (top row) and CT12 (bottom row) centroid positions in the normalized x–y reference frame. Columns correspond to the full population (left), Side nuclei (center), and Top nuclei (right). n = 150 nuclei (Side, n = 83; Top, n = 67) from three independent experiments. Statistical significance was assessed using a kernel density–based global two-sample test.

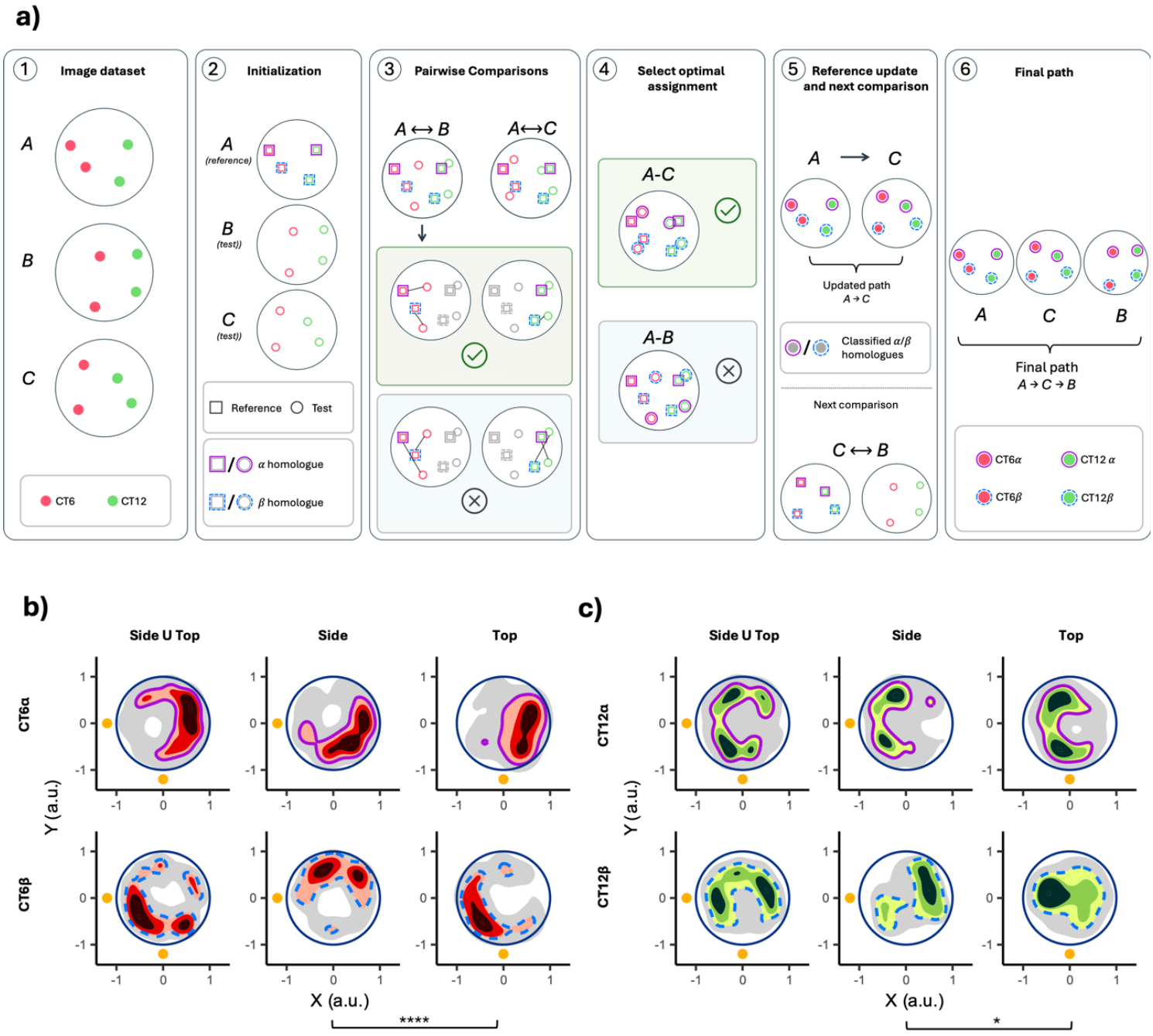


Figure 3

Homolog classification reveals distinct nuclear topological classes. (a) Schematic representation of the similarity-based algorithm used to assign homolog identities across the dataset. The procedure operates on single-cell centroid coordinates of CT6 and CT12. (step 1) For each nucleus, pairwise comparisons with all other nuclei are performed to compute spatial similarity between homolog configurations (e.g., A–B and A–C; steps 2–3). Homolog pairing is determined by selecting the configuration that minimizes positional dissimilarity (step 4). Through iterative reference updating and successive pairwise comparisons, a globally consistent α (solid purple contour) and β (dashed light-blue contour) labeling is propagated across the population (step 5), yielding the final optimal similarity path (step 6). (b) Kernel

density estimation (KDE) maps of CT6 α homologs (top row, solid purple contour) and β homologs (bottom row, dashed light-blue contour) in the normalized x–y reference frame. Columns correspond to the full population (left), Side nuclei (center), and Top nuclei (right). (c) Spatial probability maps of CT12 α (top row, solid purple contour) and β (bottom row, dashed light blue contour) homologs in normalized coordinates. Columns correspond to the full population (left), Side nuclei (center), and Top nuclei (right). n = 150 nuclei (Side, n = 83; Top, n = 67) from three independent experiments. Statistical significance was assessed using a kernel density–based global two-sample test.

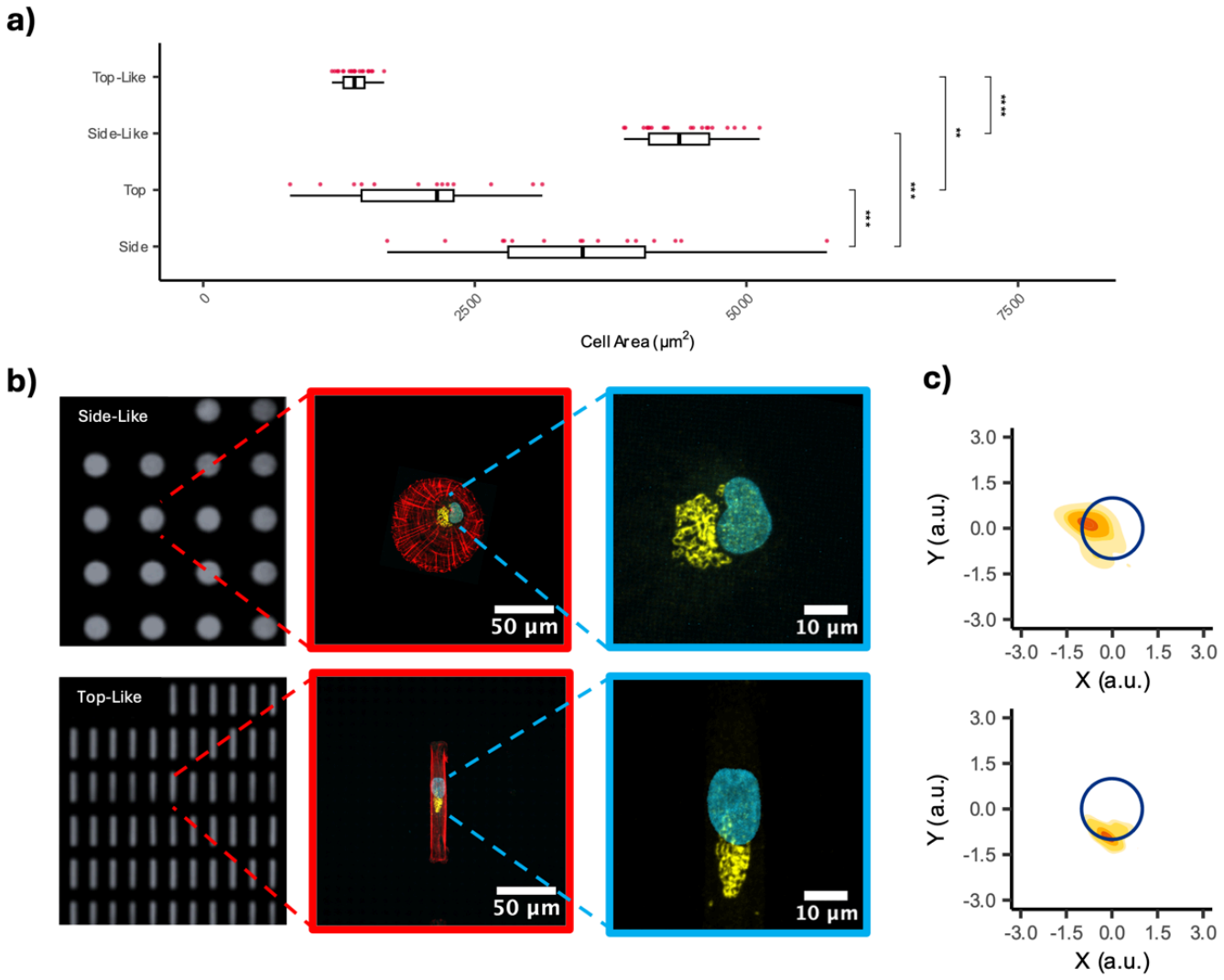


Figure 4

Micropatterned confinement recapitulates Side and Top cellular and nuclear morphology. (a) Box-and-jitter plots showing the cell spreading area across Side, Top, Side-Like (circular micropattern), and Top-Like (rectangular micropattern) hMSCs. (b) Representative confocal images of micropatterned confined Side-Like (top row) and Top-Like (bottom row) hMSCs. From left to right: fluorescently labeled fibronectin micropatterns, insets showing representative hMSCs adhered to the corresponding adhesive islands,

and merged confocal z-stack projections of nucleus (DAPI, blue), Golgi apparatus (yellow), and actin cytoskeleton (red). Scale bars, 50 μm and 10 μm. (c) Kernel density estimation (KDE) maps of Golgi centroid distributions in Side-Like (top row) and Top-Like (bottom row) nuclei, shown in the normalized x–y reference frame. n ≥ 20 cells per condition. Statistical significance between pairwise groups for panel (a) was assessed using the pairwise Wilcoxon test.

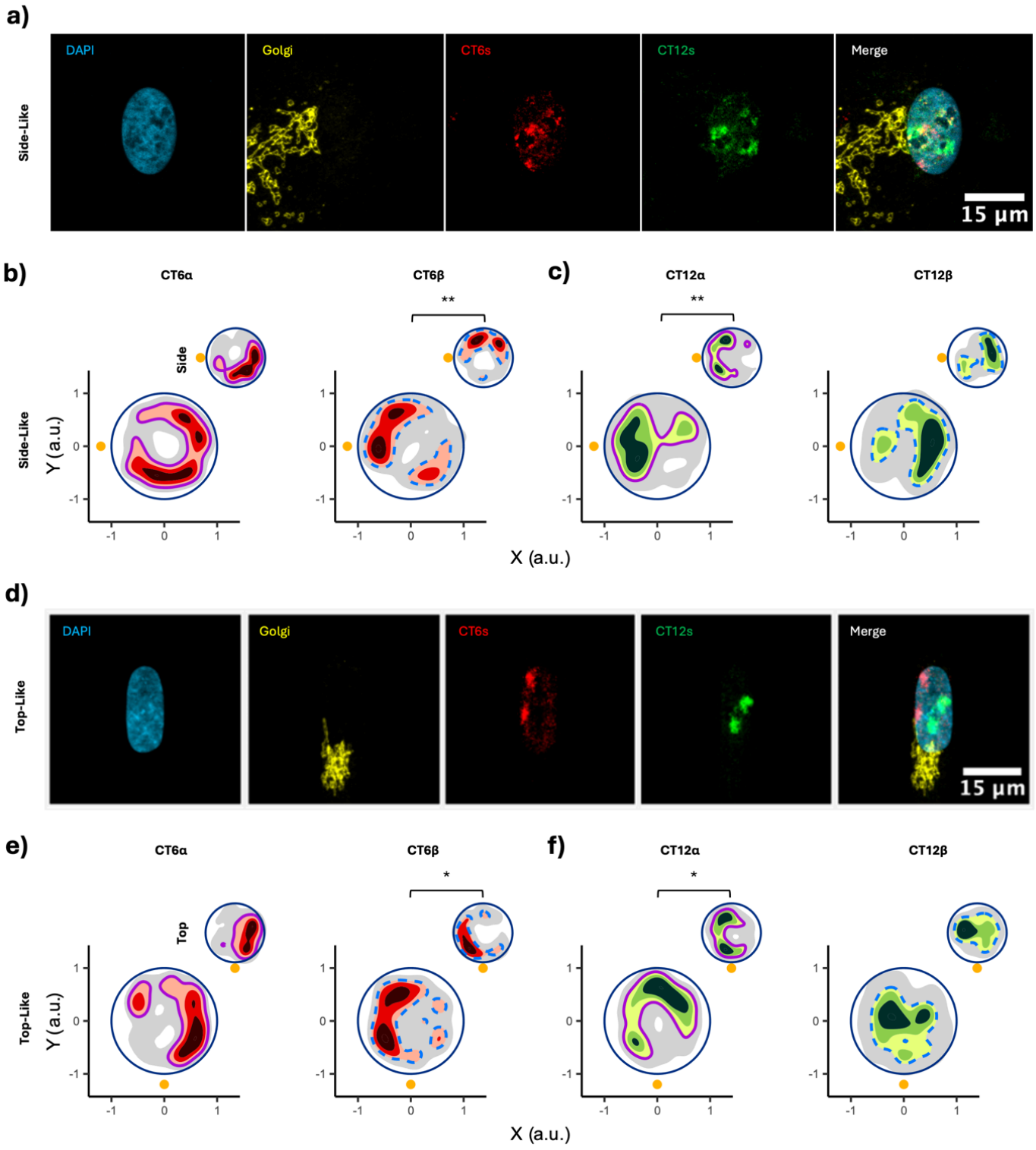


Figure 5

Side-Like and Top-Like micropatterned hMSCs recapitulate nuclear topological classes observed in unconfined cells.(a) Representative confocal images of micropatterned confined Side-Like hMSCs. From left to right: nucleus (DAPI, blue), Golgi apparatus (anti-giantin, yellow), CT6 (red), CT12 (green), and merged channels. Scale bar, 15 μm. (b) KDE maps of CT6 α (left) and β (right) homologs in Side-Like configurations compared to Side counterparts (inset). (c) KDE maps of CT12 α (left) and β (right) homologs in Side-Like configurations compared to Side counterparts (inset). (d) Representative confocal images of micropatterned confined Top-Like hMSCs. From left to right: nucleus (DAPI, blue), Golgi apparatus (anti-giantin, yellow), CT6 (red), CT12 (green), and merged channels. Scale bar, 15 μm. (e) KDE maps of CT6 α (left) and β (right) homologs in Top-Like configurations compared to Top counterparts (inset). (f) KDE maps of CT12 α (left) and β (right) homologs in Top-Like configurations compared to Top counterparts (inset). n > 50 cells (Side, n = 83; Side-Like, n = 100; Top, n = 67; Top-Like, n = 150) from three independent experiments per condition. Statistical significance was assessed using a kernel density–based global two-sample test.

Supplementary Files

This is a list of supplementary files associated with this preprint. Click to download.

- CodeanddataMessinaetal.zip
- SupplementaryInformationMessinaetal.docx